ARTICLE

Semisynthetic Ferritin-based Nanoparticles with High Magnetic Anisotropy for Spatial Magnetic Manipulation and Inductive Heating

Andreas Neusch[a], Ulf Wiedwald[b], Iuliia P. Novoselova[a,c], Daniel A. Kuckla[a], Nikolaos Tetos[b], Sarah Sadik[a,d], Philipp Hagemann[a], Michael Farle[b] and Cornelia Monzel[a,*]

The human iron storage protein ferritin represents an appealing template to realise a semisynthetic magnetic nanoparticle (MNP) for spatial manipulation or inductive heating applications on a nanoscale. Ferritin consists of a protein cage of well-defined size (12 nm), which is genetically modifiable, biocompatible, and into which a magnetic core is synthesised. Here, we probe the magnetic response and hence the MNP's suitability for (bio-)nanotechnological or nanomedical applications, when the core is doped with 7 % cobalt or 7 % zinc, in comparison to the undoped iron oxide MNP. The samples exhibit almost identical core and hydrodynamic sizes, along with their tunable magnetic core characteristics as verified by structural and magnetic characterisation. Cobalt doping significantly increased the MNP's anisotropy and hence the heating power in comparison to the other magnetic cores with potential application as a mild heat mediator. Spatial magnetic manipulation was tested with MNPs inside droplets, the cell cytoplasm, or the cell nucleus, where the MNP surface conjugation with mEGFP and poly(ethylene glycol) gave rise to excellent intracellular stability and traceability within the complex biological environment. A magnetic stimulus (smaller than fN forces) results in the quick and reversible redistribution of the MNPs. The obtained data suggest that semisynthetic ferritin MNPs are highly versatile nanoagents and promising candidates for theranostic or (bio-)nanotechnological applications.

Introduction

Over the last decades, magnetic nanoparticles (MNPs) have become indispensable tools in nanomedicine for delivery[1,2], imaging[3–6], therapy[5,7,8], or combined approaches. More recently, (bio)nanotechnology-based approaches use the specific coupling of MNPs to biomolecules to (1) inductively heat them to create nanoscale hot spots[9–11], to (2) spatially redistribute molecules[12,13], since the spatiotemporal distribution of molecules plays a key role in biological signalling processes[14,15], or (3) to apply forces to molecules for their controlled conformational change. The particular advantage of combining such nanoparticle-based approach with a remote magnetic stimulus is, to actively change biomolecular states in a contact-free and controlled manner. This is in contrast to what is hitherto possible be only observing a system's passive response. The active stimulation provided by cases (1)-(3) is highly relevant for biomaterial development, for subcellular signalling or biomechanical studies[16–19], as well as for applying a stimulus in a whole organism. The aforementioned nanomedical approaches always aim at an *in vivo* application. To use MNPs in such biological context, however, requires their biocompatibility, to endow them with specific targeting properties, a magnetic core which is sufficiently magnetisable and tuneable in regards to its magnetic anisotropy. In addition, the overall particle size should be below 100 nm.[20] As a result, partly contradictory demands need to be reconciled, which generally is a difficult task.

Here, we synthesise ferritin-based MNPs, commonly referred to as Magnetoferritin (MFt), which have attracted considerable attention due to their semi-synthetic and multifunctional nature.[21–26] We show how MFts meet most of the above mentioned demands and scrutinise their suitability for spatial magnetic manipulation and inductive heating approaches, the latter also as response to a recent discussion in the field.[27,28]
MFts are based on the natural iron storage protein ferritin, which forms a small, well-defined hollow sphere with an internal and external diameter of 8 nm and 12 nm respectively.[29,30] As such, the protein serves as a template, into which magnetic nanocrystals of high homogeneity, in terms of their shape and size, are synthesised. This semi-synthetic design using a protein shell as a template has several advantages for theranostic or (bio-)nanotechnological applications: among them are the excellent solubility and stability in physiological solutions as well as a low toxicity. Moreover, due to the well-

[a] *Experimental Medical Physics, Heinrich-Heine University Düsseldorf, 40225 Düsseldorf, Germany.*
[b] *Faculty of Physics and Center for Nanointegration (CENIDE), University of Duisburg-Essen, 47057 Duisburg, Germany*
[c] *Present address: Institute of Human Genetics, University Hospital Düsseldorf, Heinrich-Heine-University Düsseldorf, 40225 Düsseldorf, Germany*
[d] *Present address: Cell Biology and Cancer, UMR 144 CNRS, Institute Curie, 75248 Paris cedex 05, France.*
* *Corresponding author (Cornelia.Monzel@hhu.de)*

defined, small size, it remains mobile in various biological environments.[17,31,32] Further, MFts can be easily modified by genetic engineering or chemical reactions involving one of the primary amines, carboxylates or thiols exposed to their exterior. Thus, fluorescent labels or tags for site-specific targeting can be attached.[33–35] Previously, MFts were shown to couple to other biomolecules without apparent alteration of their natural function.[36–38] Finally, ferritin exhibits an exceptional stability over a wide range of temperatures (up to ~80 °C) and pH (3-10).

Ferritin is the most abundant iron-storage protein and its globular, hollow structure is conserved in most organisms. It is responsible for mediating the iron homeostasis and to prevent oxidative stress.[22] Human ferritin has a size of 12 nm in diameter and is a 24-mer[39] composed of two subunits: heavy chain (HCF) and light chain ferritin (LCF).[22,40] Due to structural similarities, cages can be formed by any numerical combination of the two subunits. Although LCF and HCF are almost identical in structure, only HCF is equipped with a ferroxidase domain capable of oxidising toxic, soluble Fe(II) to the insoluble and less harmful Fe(III) upon intake. The oxidised iron atoms sediment inside the cage and can fill it up to approximately 4,500 iron atoms.[41] Naturally occurring ferritin cores are ferrihydrites and were reported to exhibit paramagnetic or superparamagnetic properties above 12K.[42]
With regard to the core, a wide choice of inorganic materials have so far been mineralised inside the ferritin cage, such as Fe_3O_4 [43–46], Co_3O_4 [47,48], Mn_3O_4 [49], CoPt [50], Pd [51], Ag [52], CdS [53], CdSe [54], and ZnSe.[55] Here, the inner cage diameter of 8 nm naturally confines the core and gives rise to a narrow size distribution. The synthesised MNPs are generally superparamagnetic at ambient or higher temperature, as they exhibit a magnetocrystalline anisotropy with an energy density that cannot block the particle's magnetic dipole moment at an upper size limit of 8 nm given by the Ferritin cage. Superparamagnetism is particularly advantageous in many applications, since the nanoparticles do not show significant particle-particle (magnetic dipole-dipole) interaction. As a result, they do not form chains or aggregates in suspension and are more stable over time. On the other hand, the constraint to the growth of the inorganic core imposed by the ferritin size represents an important limitation to its magnetic properties. In particular, the applicability of ferritin for the hyperthermic heating of malignant cells or for the switching of thermally sensitive molecules was recently questioned.[27] Theoretical and experimental studies have indeed demonstrated that the maximum efficiency of hyperthermic heating is reached for magnetite MNPs of 15-18 nm diameter and that it drops off sharply upon MNP size reduction.[19,56–59]

It is hence important to show that the MFts' properties can be tuned to maximise their efficiency for hyperthermic heating as well as their suitability for spatial magnetic remote manipulation. A viable route is to increase the magnetic anisotropy of the inorganic core, which can be simply realised through the replacement of ferrous ions in the Fe oxides with dopants.[11] A prominent example are cobalt doped ferrite nanoparticles, whose magnetocrystalline anisotropy can be up to 20 times larger compared to the undoped ferrite, retaining a good heat dissipation property down to the size of about 8 nm.[60] Interestingly, the highest values of magnetic anisotropy in ferritin were previously obtained using cobalt (Co) doping of a few percent.[31,61,62] When ferrite nanoparticles were doped with a few percent of zinc (Zn), the saturation magnetisation was shown to increase slightly.[63] Additional changes in the magnetic behaviour of the particles may arise, due to the inverse spinel structure of Co doped ferrites (with Co^{2+} ions in octahedral sites and Fe^{3+} ions equally distributed between tetrahedral and octahedral sites) and the normal spinel structure of Zn doped ferrites (with Zn^{2+} ions in tetrahedral and Fe^{3+} in octahedral sites).[64] On the basis of these findings, we here investigate the effect of doping MFt cores with 7 % Co or 7 % Zn with respect to Fe as a possible strategy for improved spatial manipulation and magnetic hyperthermia, to fully exploit the multiple advantages that ferritin MNPs offer.

In this work, first, the structural and magnetic properties of three different MFts are determined. Thereafter, an example to increase the MFts' inductive heating response is presented. The spatial manipulation of MFts applying magnetic field gradients is then shown for simple droplets and inside living cells. In the cell cytoplasm as well as in the cell nucleus, a repetitive and reversible tuning of MFts spatial distributions is achieved. Overall, the comparison of different MFts and their applications provide important guidelines for their use as biomedical or nanotechnological agents.

Materials & Methods

Ferritin Purification.

The semi-synthetic ferritin nanoprobe was prepared as previously described.[32] In short, the ferritin cage was genetically engineered so that each subunit of the 24-homomer consisted of the heavy chain ferritin subunit N-terminally fused to mEGFP. The cDNA of this fused subunit was inserted into the pET21a vector (reporter gene: *ampR*, see Figure S1). The construct was a generous gift from the Coppey/Hajj laboratory at the Laboratoire Physico-Chimie, Institut Curie, Paris, France and the Piehler laboratory at the University of Osnabrück, Germany.
The engineered protein was expressed in BL21-CodonPlus (DE3)-RIPL Competent Cells (Agilent, Santa Clara, CA, USA). Bacteria were transformed via heat shock and plated on LB-Agar containing ampicillin (0.1 µg/mL). A single colony was picked and used to grow a preculture and later the main culture in 2xYT medium (containing 0.1 µg/mL ampicillin). Bacteria were grown at 37 °C and 230 rpm in an orbital shaking incubator up to an OD_{600} of 0.6 to 0.8. At this point, expression was induced by the addition of the lac operon activator IPTG (isopropyl β-d-1-thiogalactopyranoside) at a final concentration of 1 mM. Cultures were incubated for 16 h at 16 °C and 160 rpm in a shaking incubator. Bacteria were then harvested at 8,000 g for 10 min, washed in PBS, collected at 19,000 g for 5 min and

finally resuspended in HEPES-2 buffer (50 mM HEPES, 150 mM NaCl, pH 8.0, filtered 0.2 µm). To prevent unwanted protein degradation, protease inhibitors were added to the bacteria (cOmplete EDTA-free Protease Inhibitor Cocktail, Roche, Basel, Switzerland). Bacteria were homogenised in a microfluidiser (M110P Microfluidizer, Microfluidics, Westwood, MA, USA). After cell disruption, PMSF (phenylmethylsulfonyl fluoride) was added to the solution at a final concentration of 5 mM. The lysate was then centrifuged for 40 min at 19,000 g and 4 °C. The released proteins were further purified by heat denaturation in a water bath at 70 °C for 15 min and ammonium sulphate precipitation at 30 % and 70 % at 4 °C. After desalting via dialysis (20 kDa cut-off) against buffer HEPES-1 (20 mM HEPES, 100 mM NaCl, pH 8.0, filtered 0.2 µm), the protein solution was separated using a size exclusion column (HiPrep Sephacryl S-400 HR, Cytiva, Marlborough, MA, USA) in a FPLC system (NGC, Bio-Rad, Hercules, CA, USA). The purified ferritin cages were then PEGylated using O-[(N-Succinimidyl)succinyl-aminoethyl]-O'-methylpolyethylene glycol 2'000 (Sigma Aldrich, St. Louis, MO, USA) in DMSO at a molar excess of 3,500 PEG units per ferritin cage. The mixture was left to react at room temperature for 2 h on a rotary shaker and was cleaned afterwards using a PD-10 desalting columns (Cytiva).

Magnetic Core Synthesis.

Ferritin was loaded with a magnetic core, consisting of ferrihydrite including Cobalt or Zinc as dopants. For the synthesis, 25 mL of PEGylated ferritin was heated to 65 °C in 100 mM NaCl at a ferritin concentration of 50 nM. The pH was kept constant at 8.5 by addition of 100 mM NaOH via an autotitrator (Titration Excellence T5, Mettler-Toledo, Columbus, OH, USA). The whole reaction was performed under a constant stream of N_2, to suppress unwanted oxidation.

To produce doped magnetic cores, 2 mL of both the metallic precursor mix (see Table 1) and H_2O_2 (5.5 mM, Merck, Darmstadt, Germany) were added to the reaction vessel at a rate of 200 µL/min. After addition, the reaction was quenched with sodium citrate at a final concentration of 2 mM. The fresh product was centrifuged at 19,000 g at 4 °C for 30 min, then filtered through a 0.2 µm syringe filter and concentrated using Amicon Ultracentrifugal filters (100 kDa cut-off, Merck).

For further characterisation of the MNPs (X-ray Diffraction and Vibrating Sample Magnetometry), samples were dialysed against low concentrated HEPES buffer (0.2 mM HEPES, 1 mM NaCl, pH 8.0) to reduce the amount of salt and buffering agent in the sample.

Table 1 – Doping of Magnetoferritin prepared from ammonium iron(II) sulphate hexahydrate ($(NH_4)_2Fe(SO_4)_2 \cdot 6H_2O$) precursor for Fe, Cobalt(II)-chloride ($CoCl_2$) for Co, and Zinc chloride ($ZnCl_2$) for Zn. All precursors are dissolved in degassed 100 mM NaCl.

Sample	Dopant	Molarity of precursor		Final %
		Fe (µM)	Dopant (µM)	
Pure	-	1034	-	-
Zn7	Zn	983	52	6.7 ± 1.3
Co7	Co	983	116	6.4 ± 2.2

Samples were then plunge frozen in liquid nitrogen and lyophilised. For all other characterisations, the samples were kept in HEPES-1.

Transmission Electron Microscopy.

Protein cages and magnetic cores were imaged with transmission electron microscopy (TEM). Cages and cores were recorded separately, since organic material such as proteins are hardly visible by TEM. Protein cages were hence stained with uranyl acetate, while magnetic cores were recorded without additional staining.

For TEM measurements, freshly prepared samples of both ferritin and differently doped Magnetoferritin (MFt) were diluted to 0.05 µM. A droplet was placed on a TEM grid (Ni grid, Formvar Carbon Film, Plano GmbH, Wetzlar, Germany) and left to sediment for 1 min. Excess solution was removed using filter paper. Unstained samples were left to dry in ambient conditions. For uranyl acetate staining, the grid was dipped into a drop of 2 % uranyl acetate for 3 s after sample sedimentation and remaining liquid was removed using filter paper. Afterwards, the grid was placed onto a second drop of 2 % uranyl acetate and left for 30 s. Excess solution was removed using filter paper and the grid left to dry in air.

Stained images were taken with a JEOL JEM-2100Plus (Akishima, Tokyo, Japan) with an acceleration voltage of 80 kV. Unstained bright-field (BF) high resolution TEM (HRTEM) and scanning TEM (STEM) images were acquired with a JEOL 2200FS transmission electron microscope at an acceleration voltage of 200 kV using a 2k×2k GATAN UltraScan1000XP CCD camera. The local chemical composition was determined using EDX in STEM mode with an Oxford windowless 80 mm^2 SDD X-MaxN 80 TLE detector with 0.21 sr solid angle. HRTEM and EDX data were analysed using Gatan Micrograph Suite and Oxford's Aztec software.

X-ray diffraction (XRD).

XRD patterns were measured in a PANalytical X'Pert PRO diffractometer equipped with a spinner for powders using Cu-K_α radiation and the X'Celerator detector. The background of the XRD patterns was subtracted and further data processing was performed using OriginPro. A 50-point moving average smoothing was applied to the diffractograms. Due to the small step width, the MFt peak width remained unchanged while the sharp NaCl peaks exhibit slightly smaller intensities.

Vibrating Sample Magnetometry (VSM).

The magnetic properties of all samples were studied via Vibrating Sample Magnetometry, VSM, in a PPMS DynaCool system (Quantum Design, San Diego, CA, USA). The measurements were taken on powder samples within the field range of ±9 T at various temperatures, ranging from 5 K to 330 K and were normalised to the total sample mass.

Dynamic Light Scattering and Electrophoretic Light Scattering.

For characterisation of nanoparticles in solution and, hence, under biological conditions, Magnetoferritin was analysed using Dynamic Light Scattering (DLS) and Electrophoretic Light

Scattering (ELS). Prior to measuring, samples were diluted to 1 µM in HEPES-1 buffer (pH 8.0, see section Ferritin Purification) and filtered through a 0.2 µm filter to remove agglomerates. All measurements were performed on a Zetasizer Nano ZS (Malvern Panalytic Ltd., Malvern, UK). Each sample was characterised by averaging over 75 sub-runs (5 subsequent runs, each containing 15 sub-runs) with 10 s measurements per sub-run. A log-normal fit was applied to the measured number distribution to calculate the hydrodynamic diameter D_H, representing the diameter of a sphere with the same diffusion properties as the analysed particle.

ELS measurements were performed at 40 V to account for the high conductivity of the saline buffers and to prevent damage of the measuring cell's electrodes. For each sample, 300 sub-runs (10 subsequent runs, each containing 30 sub-runs) were recorded.

Alternating magnetic field-induced heating.

Magnetic hyperthermia measurements were performed in a custom-made alternating magnetic field (AMF) setup described before.[65] In short, 200 µL of Magnetoferritin solution was placed in a single-use cuvette and subjected to an AC magnetic field (45 mT induction amplitude at 93.75 kHz or 104.5 kHz). Thermal changes were monitored recording the solution surface with a thermal imager (VarioCam HD, Infratec GmbH, Dresden, Germany) with an IR 1.0/30 JENOPTIK objective (Infratec GmbH). Measurements were performed every 10 s over a duration of 30 min. The magnetic field was switched on directly after the first image and switched off after 15 min (91 images). To obtain the sample's temperature, the average temperature of the sample surface in the cuvette (approximately 5 x 10 mm² or 300 pixels) was determined. The measurement was repeated three times for all samples. Images were evaluated with the software IRBIS 3 plus (Infratec GmbH).

Droplet Assay for Quantification of Magnetic Forces.

In order to characterise the forces that can be applied to MFt, a droplet assay on coverslips was performed. In a first step, coverslips were coated with a PDMS layer (SYLGARD 184 Silicone Elastomer Kit, Dow Europe GmbH, Wiesbaden, Germany) to reduce unspecific binding of MFt to the glass surface. For this, a 1:10 mixture (curing agent to elastomer by weight) of PDMS was diluted in twice the amount (by weight) of hexane.[66] A coverslip (22 x 22 mm², thickness: 170 ± 5 µm) was sonicated in an ultrasonic bath for 10 min in isopropanol, followed by another sonication in ultrapure water. In between treatments, the coverslip was thoroughly flushed with ultrapure water. Afterwards, the coverslip was blown dry using pressurised N_2. The coverslip was then mounted onto a spin coater and 100 µL of the PDMS mixture was placed on top. The spin coater was run for 150 s at 6,000 rpm with an acceleration of 100 rpm/s. After spin coating, the coverslip was cured at 110 °C for 20 min.

For the droplet assay, MFt was diluted to 0.1 µM in HEPES-1 with 25 V-% of glycerol. A droplet of 1 µL was placed onto a PDMS-coated coverslip and a magnetic tip was approached. The magnetic tip consist of two magnets (cube: NdFeB, side length 5 mm, gold-plated, product number W-05-G; cuboid: NdFeB, 10 × 4 × 1.2 mm³, gold-plated, product number: Q-10-4-1.2-G; both from supermagnete.de by Webcraft GmbH, Gottmadingen, Germany) and a steel wire (diameter: 0.4 mm, product number 1416, Röslau Stahldraht, Röslau, Germany) attached to the magnets.[32] The attraction of the fluorescent MFt was observed using an inverted epifluorescence microscope (IX83 by Olympus, Shinjuku, Tokyo, Japan) equipped with a 60x oil-objective with a numerical aperture N.A. = 1.25. Data analysis was performed using Matlab (R2023a, The Mathworks Inc., Natick, MA, USA). A horizontal line scan (thickness 1 µm) over the intensity in the fluorescence channel was done starting from the position of the magnetic tip. Position 0 was placed at the edge of the drop with the inside of the drop in the positive direction. A linear background ($\boldsymbol{y = mx + c}$) was fitted to intensities at higher positions and subtracted from the line scan to obtain the final intensity curve.

Spatial magnetic manipulation.

For imaging and manipulation, Cos7 cells were plated on sterilised glass coverslips in 35 mm cell-culture dishes at about 50 % confluency. Prior to experiments, cells were washed with PBS buffer and re-incubated in preheated Leibovitz medium (L15, Thermo Fisher Scientific, Waltham, MA, USA), supplemented with 10 % foetal calf serum (FCS) and 1 % PenStrep (Thermo Fisher Scientific). Imaging was performed in a heating chamber (TempController 2000-2, PeCon GmbH, Erbach, Germany) set to 37 °C and mounted on an inverted microscope (IX83 from Olympus, Shinjuku, Tokyo, Japan) equipped with a 60x oil-objective with N.A. = 1.25 and phase contrast PH3 (Olympus UPLFLN60XOIPH/1,25, Olympus K.K., Shinjuku, Japan). MFts were centrifuged (10,000 g for 10 min) and the supernatant was used. MNPs were injected into cells using a micromanipulation system (InjectMan 4 and FemtoJet 4i, Eppendorf, Hamburg, Germany) with microinjection capillaries (Femtotip II, inner diameter of 500 nm, Eppendorf, Hamburg, Germany). For injection, a concentration of 1 µM of MFt was used. After microinjection, the sample was washed with the previously mentioned Leibovitz medium to remove remaining MFt in the medium. Thereafter, a home-built magnetic tip (described in section Droplet Assay for Quantification of Magnetic Force and in Novoselova *et al.*[32]) was approached to the cell using the InjectMan 4 of the micromanipulation system. Videos of MFt redistribution in the fluorescence channel were acquired typically every 10 s over 30-45 min at 200 ms camera exposure time (Prime BSI, Photometrics, Tucson, AZ, USA, see also SI Video S1-S3). Phase contrast and fluorescence image recordings were analysed using inhouse developed analysis routines written in Matlab (R2023a, The Mathworks Inc., Natick, MA, USA) and ImageJ (version 1.49v, U. S. National Institutes of Health, Bethesda, MD, USA).[67] A background subtraction was applied to the fluorescence videos.

Results & Discussion

Magnetoferritin (MFt) poses a highly interesting nanoagent for spatial redistribution studies in external magnetic fields and has been controversially discussed as candidate to mediate inductive heating processes.[27,31,68] Here, we probe the MFt's characteristics and dope the magnetic core to tailor its magnetic properties (*i.e.,* increase the magnetic anisotropy energy density and saturation magnetisation) for these applications.

Synthesis and Structural Characterisation.

A set of three MFts was prepared using a ferritin cage based on only HCF subunits fused N-terminally to mEGFP. For the magnetic core synthesis, either pure Fe^{2+}, or Fe^{2+} doped with a final doping ratio of 7 % (mol/mol) Co^{2+} or doped with 7 % (mol/mol) Zn^{2+} with respect to the total metal amount was used (see Figure 1, Figure 2, and Table 1). The dopant molarity used during the synthesis was a few percent higher (see Materials and Methods), but effectively gave rise to the 7 % doping reported here (see also Figure 3). The biomineralisation reaction was carried-out inside the purified and PEGylated ferritin. The obtained MFts were first characterised by transmission electron microscopy (see Figure 1 and Figure 2) and dynamic light scattering to probe the protein and core size, respectively.

The mean diameter of all MFt cages measured with TEM was 13.9 ± 2.2 nm (see Figure S2), whereas the mean hydrodynamic diameter of MFts measured with DLS was 36.7 ± 1.9 nm for pure, 44.7 ± 3.3 nm for Co^{2+} doped, and 43.4 ± 7.1 nm for Zn^{2+} doped MFt (Figure 1 and Table 2). The polydispersity index was ≤ 0.17 for all MFts, confirming the expected small size distribution within the sample (Table 2). The diameter values are in accordance with previous reports,[32] where the TEM size of the protein structure matches the theoretical calculation of the mEGFP decorated protein diameter (12+2×2.3 = 16.6 nm).[69] The larger hydrodynamic size in comparison to the physical size was typically observed after surface PEGylation and core synthesis, giving rise to an increased hydrophilicity. This effective hydrodynamic diameter is particularly suitable for subcellular applications, since cytoplasmic non-specific interactions between a nanoprobe and the proteins/fibres in the cytoplasm dramatically increase above 50 nm, as previously reported.[13,70] In addition, the measured negative ζ-potential of around -5 mV (Table 2) prevents non-specific interactions within the primarily negatively charged biological environment. The mean diameter of all cores was 6.3 ± 1.8 nm (Figure 2), which is in accordance with previously reported values of synthetically loaded ferritin cages.[17,32] There were no systematic differences in size after loading the cages with Fe, or together with Co or Zn as dopants. Reproducibility of the magnetic core synthesis was evaluated by three separate syntheses (called runs in the following) and analysed separately, unless stated otherwise.

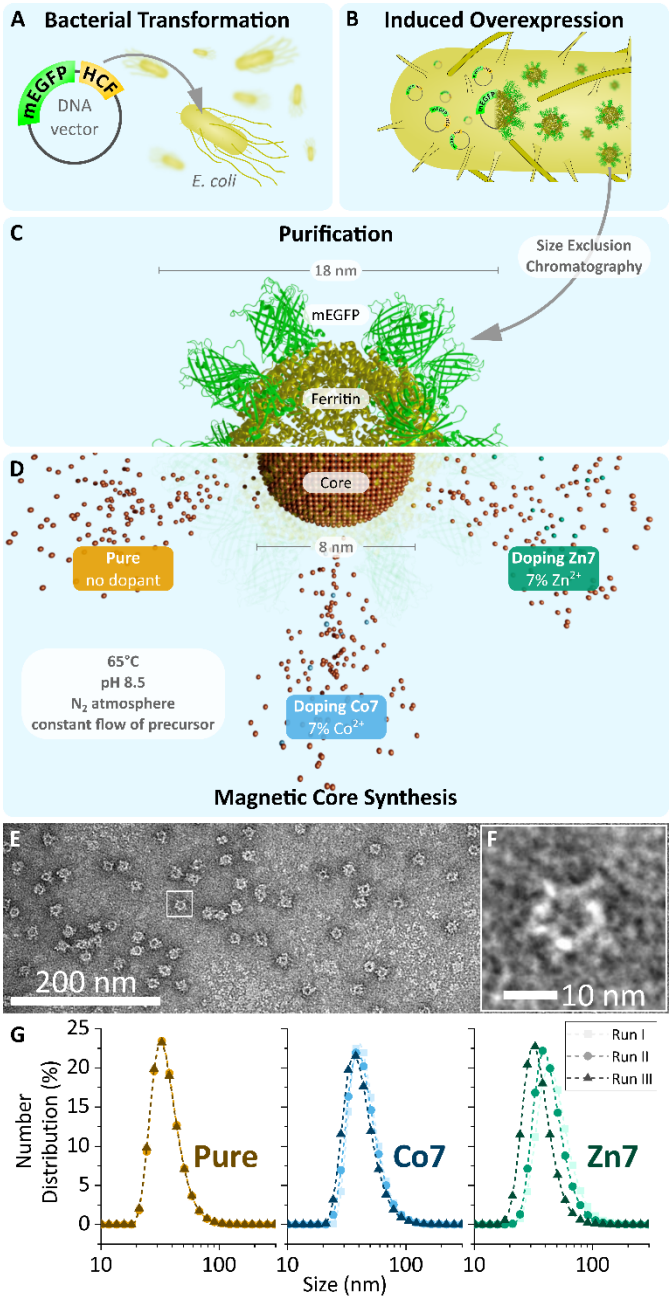

Figure 1 – (A-D) Schematic overview of MFt production. Apoferritin (yellow), genetically fused to mEGFP (green), is expressed in transformed *E. coli* and then purified via size exclusion chromatography. Empty cages are filled with their respective metal oxide core (brown) during magnetic core synthesis. (C and D) Scheme of semi-synthetic MFt cage. The three different cores used in this study are indicated. (E) Transmission electron microscopy image of pure MFt's protein shell, stained with 2 % uranyl acetate. (F) Magnified section of E displaying one single ferritin cage. (G) Hydrodynamic radii obtained via dynamic light scattering for MFt with three differently doped cores over three independent synthesis runs.

Table 2 – Properties of doped MFts. D_H: Hydrodynamic Diameter, PdI: Polydispersity Index, both obtained from DLS measurements. For more details see Table S1.

Sample	D_H (nm)	PdI	ζ-Potential (mV)
Pure	36.7 ± 1.9	0.16 ± 0.01	-5.1 ± 0.7
Co7	44.7 ± 3.3	0.17 ± 0.02	-4.7 ± 1.1
Zn7	43.4 ± 7.1	0.17 ± 0.01	-4.8 ± 0.8

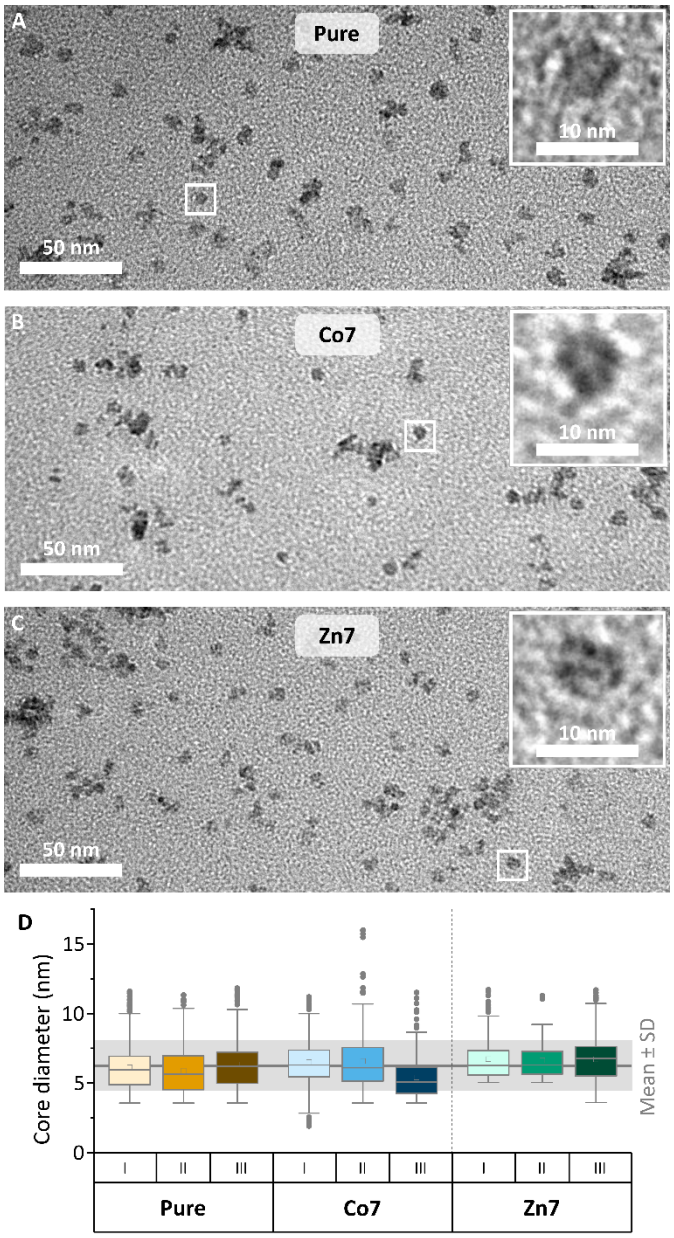

Figure 2 – (A-C) Transmission Electron Microscopy images of Magnetoferritin. Images of all doping conditions were taken without staining to visualise metallic cores. (D) Box plots show diameter of cores from three independent synthesis runs (I, II and III) of all three doping conditions (each N ≥ 93; Mean ± SD = 6.3 ± 1.8 nm). Mean values are shown as boxes, median values as horizontal lines.

The doping level of Co and Zn was determined by energy dispersive X-ray spectroscopy in scanning transmission electron microscopy (EDX-STEM). Figure 3 shows high-resolution STEM images in the upper row, along with Fe, Co, and Zn elemental maps in the middle and lower row. High-resolution STEM images appear blurry, due to the organics surrounding the magnetic cores. Under the focused electron beam, significant amounts of amorphous carbon were growing, thus limiting the resolution and acquisition time for elemental maps of Fe, Co, and Zn. Nonetheless, individual cores are visible in the pure MFt samples, while core accumulations yielded larger EDX signals.

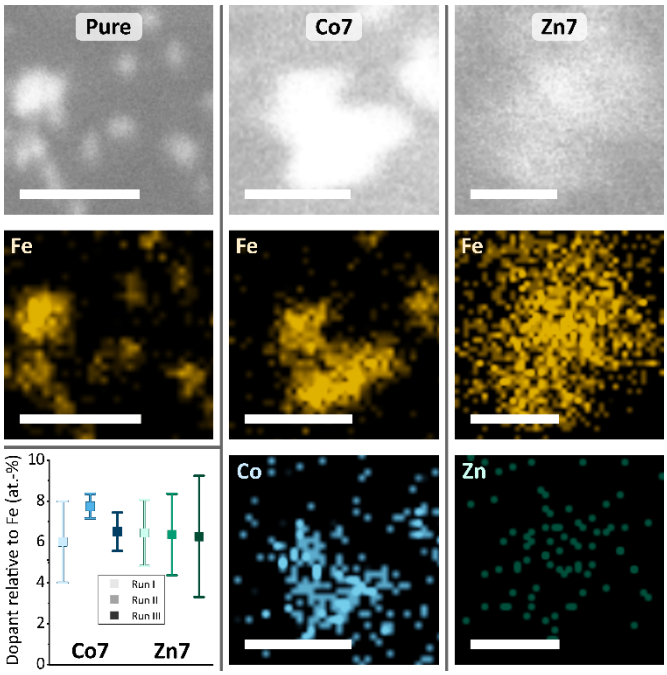

Figure 3 – (A) Representative EDX-STEM images of MFt (Pure) and doped (Co7, Zn7) samples. (B) Elemental maps for indicated elements Fe, Co, and Zn (scale bar: 50 nm). (C) The graph shows the dopant concentration relative to Fe of individual runs I-III.

The elemental maps in Figure 3 clearly show the colocalisation of Co or Zn with Fe. For the quantification of Co and Zn doping levels with respect to Fe, more than ten EDX spectra, each over small areas, were measured including about 20-30 magnetic cores. The results of each run are summarised in the graph in Figure 3. The desired low doping levels of 6.8 ± 1.3 at.-% for Co and 6.4 ± 1.9 at.-% for Zn relative to the Fe intensity in the EDX spectra were obtained**,** with error bars indicating their standard deviation. All three individual runs of Co doped (from now on called Co7) or Zn doped (Zn7) samples contained only cores with doping elements, excluding the presence of pure iron or cobalt and zinc oxide. At this point we can state, that Co and Zn doping of MFt cores is possible and reproducible, with a quite homogeneous distribution of dopants from core-to-core.

To further investigate the crystal structure of the MFts, we used X-ray diffraction. The three individual samples for each dopant (Runs I-III) were pooled, to increase the signal intensity. Since the small size of the MFts and the large amount of organic material gave rise to a background signal, Figure 4 presents the X-ray diffractogram using Cu-K_α radiation after background removal and smoothing.

Overall, the diffractograms of pure and doped MFt samples are similar and consist of a set of sharp and broader peaks. The sharp peaks (indicated by asterisks) originate from NaCl crystallising during the drying process. However, more interesting are the broader peaks reflecting the diffractogram of few-nm crystallites, *i.e.,* the pure MFt and Co7 and Zn7 doped samples. The crystallite sizes of 3-4 nm given in Figure 3 were evaluated from the two largest peaks of each diffractogram using Scherrer's approach.[71]

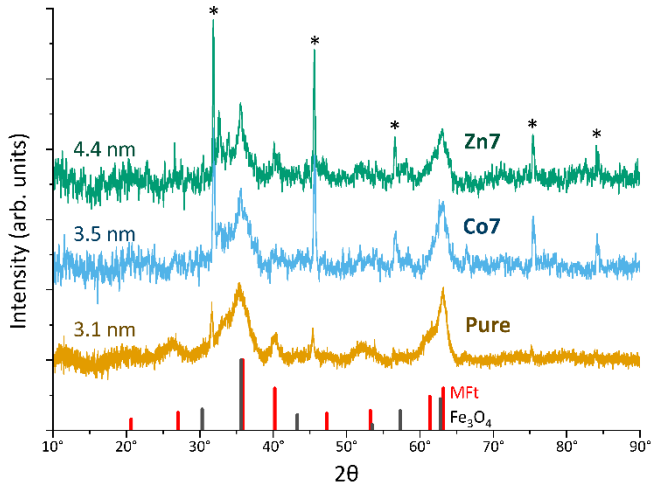

Figure 4 – X-ray diffraction of Magnetoferritin (Pure) and doped (Co7, Zn7) samples using Cu-K_α radiation. Runs I-III were pooled. Sharp peaks indicated by asterisks originate from residual NaCl after drying. Crystallite sizes from Scherrer analysis are given on the left. Sticks in black and red indicate the angles and intensities for Fe_3O_4 and MFt powder samples, respectively. Diffractograms are shifted vertically for better visibility.

Considering the average core diameter of 6.3 nm and 3-4 nm crystallite sizes, each MFt is estimated to consist of 4-9 crystallites regardless of doping. These numbers are realistic in light of the number of the HCF crystallisation points in a cage.[72] The diffractograms have close relation to the one of 6-line ferrihydrite[73,74] while ferrites including the often-observed ferrimagnetic magnetite (Fe_3O_4) or maghemite (Fe_2O_3) can be excluded from the peak positions and relative intensities. For this comparison, powder-like samples[75,76] were assumed and the patterns of standard bulk cobalt ferrite (PDF-*00*-0221086), magnetite (PDF-00-019-0629) and maghemite (PDF-00-039-1346) were used. While different structures of ferrihydrite have been suggested over the decades, it is clear from previous studies that defects and relative site occupancies slightly modify the XRD response.

Magnetic Characterisation.

The structural characterisation of the MFts in terms of component sizes and core composition showed a high homogeneity and similar properties between the three different samples. Any change in terms of their suitability for spatial manipulation and inductive heating approaches should thus depend on their magnetic properties. In Figure 5A, the zero field-cooling (ZFC) and field-cooling (FC) magnetisation curves at B = 5 mT are displayed. For direct comparison of the blocking temperature, all curves are normalised to the FC value at T = 5 K. For clarity, we show only one curve for the pure MFt, and the Co7 and Zn7 doped samples as indicated by run number, while the values given below are accompanied with the statistics of the three independent runs. All individual runs confirm the trends. It is obvious from Figure 5A that both, the ZFC/FC maximum and the irreversibility point, shift with doping towards higher temperatures reflecting an increased magnetic anisotropy energy density (MAE) at constant volume given by the MFt nanocompartments (*cf.* Figure 2D). Taking the ZFC maxima as a measure of the blocking temperature T_B we obtain 35 ± 5 K for pure MFt, 130 ± 37 K for Co7 and 74 ± 14 K for Zn7. The statistics hereby also reflects the individual doping levels achieved (*cf.* graph in Figure 3). For pure MFt in our semisynthetic approach, T_B = 35 K is about 3 times higher than usually observed for horse spleen ferritin (T_B = 10 K)[6] likely signalling different crystallisation mechanisms. While Zn doping doubles T_B as compared to pure MFt, it is striking that a low Co doping of 7 % significantly increases the blocking temperatures to 130 K and thus the effective MAE K_{eff} correspondingly, T_B can be translated in K_{eff} for single domain nanoparticles via

$$\ln\frac{\tau}{\tau_0}\, k_B T_B = A \cdot k_B T_B = K_{\mathrm{eff}} V.$$

Here, k_B is Boltzmann's constant and V the particle volume. The prefactor $A = \ln(\tau/\tau_0)$ accounts for the measurement time (for VSM 1 s) with respect to the inverse of the intrinsic attempt frequency (typically 10^{-9} s). Using a prefactor A of 21 for VSM, K_{eff} is $0.8{\cdot}10^5$ J·m^{-3} for pure MFt, $2.9{\cdot}10^5$ J·m^{-3} for Co7 and $1.6{\cdot}10^5$ J·m^{-3} for Zn7 assuming a constant volume of V = 131 nm^3. Such 3.5 times larger T_B is very attractive for inductive heating since the increased anisotropy may lead to blocking effects at frequencies of 100 kHz at constant particle volume and thus to higher heat losses via Néel relaxation processes. A rough estimate can be drawn when comparing the prefactors A_{VSM} = 21 for VSM and A_{ind} = 9 for inductive heating at 100 kHz. Then, we expect a $T_B^{100\ \mathrm{kHz}}$ = 21/9 · T_B ≈ 303 K for inductive heating experiments. Thus, hysteresis losses can be expected at 100 kHz leading to better heating in magnetic hyperthermia. Note, that this estimate assumes a frequency-independent magnetic susceptibility which is generally not the case.

Further, we discuss the important features (1) magnetisation and (2) coercive field dependence on doping. Figure 5 presents hysteresis loops at (B) T = 5 K and (C) T = 300 K. All curves are normalised to the total mass of the dried sample powder including the organic shell and residual salts. For the whole particle, we obtain magnetisations of 7-13 Am^2·kg^{-1} in B = 9 T and, as expected, the values decrease with increasing temperature. However, we cannot define the saturation magnetisation with regard to the magnetic cores only, since the magnetic content is not exactly known. Instead, we use Langevin fitting as discussed below. None of the hysteresis loops reaches saturation, which points to additional paramagnetic Fe salts or antiferromagnetic contributions in the MFt MNPs. Taking the saturation magnetisation of 6 nm Fe_3O_4 MNPs of 45 (30) Am^2·kg^{-1} at T = 5 K (300 K)[59] as an upper limit, we obtain at a ferrimagnetic fraction of at least 20-50 mass-% in the samples. This is also in line with XRD measurements showing sharp peaks (large crystallites) of NaCl after drying (*cf.* Figure 4) giving a significant contribution to the total mass.

The coercive fields $\mu_0 H_C$ at T = 5 K are 99 ± 29 mT for pure MFt, 977 ± 64 mT for Co7 and 35 ± 4 mT for Zn7. These results follow earlier studies showing a magnetic softening and higher magnetisation for Zn doped ferrites and strong hardening at slightly reduced magnetisation for Co doped ferrites.[77,78] At 300 K, all MNPs show superparamagnetic response as expected. MFts can thus be treated as single domain and weakly interacting particles following the Néel-Brown model.[79]

Finally, the magnetisation of the MNPs can be extracted from Langevin fitting of the superparamagnetic magnetisation at T = 300 K. Figure S3 presents the results for pure MFt and Co7 samples. Here, we use the Langevin function and an additional

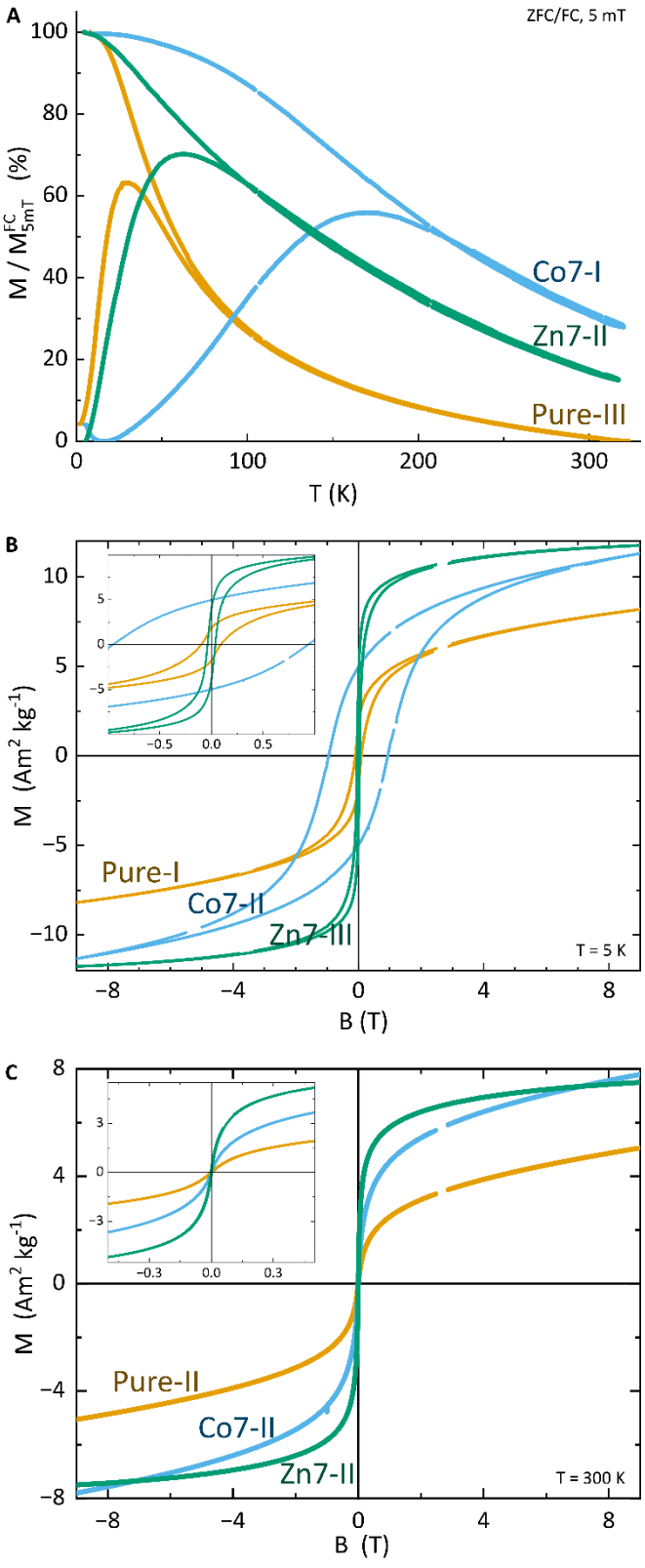

Figure 5 – Magnetometry results of pure, Co7 and Zn7 doped samples. The run number behind the doping condition reflects the individual sample. Statistics are given in the text. (A) ZFC/FC curves in B = 5 mT. (B) Hysteresis loops at T = 5 K and (C) superparamagnetic response at T = 300 K. Insets show magnification at the origin in identical units. Voids in the curves are a technical feature of the VSM resetting the sample position by a touchdown to the end position switch giving no data while the field is constantly swept.

linear slope accounting for add-on contributions of salts, organics and possible antiferromagnetic contributions in the samples. For simplicity, we fit the data with a single parameter in the Langevin function omitting the distribution of the product of magnetisation and volume. The resulting volume magnetisation are 2824 ± 704 μ_B per particle (200 ± 50 kA·m^{-1}) for pure MFt, 2973 ± 931 μ_B per particle (211 ± 66 kA·m^{-1}) for Co7 and 5620 ± 3611 μ_B per particle (398 ± 255 kA·m^{-1}) for Zn7. Pure MFt and Co7 yield similar values which are about 40 % of the bulk Fe_3O_4 magnetisation at ambient temperature. For Zn7, the larger value and larger variation of the fitting results of the three independent runs are ascribed to the larger number of agglomerates in Zn7 (*cf.* Figure 2).

For further use of doped MFt in biomedical applications, magnetometry suggests that all the generated MNPs exhibit magnetisation values suitable for spatial manipulation in external fields. For applications in magnetic hyperthermia, however, especially the Co doped MFts appear suitable due to their enhanced MAE leading to magnetic blocking close to ambient temperature. This behaviour is consistent with the substitution of Co ions for Fe ions , since the cobalt is well-known to increase the magneto-crystalline anisotropy and correspondingly, the blocking temperature.[31,61,80]

Magnetic Hyperthermia.

The heating capabilities of the MNPs were evaluated by recording the temperature kinetic curves and the hyperthermic efficiency. To this end, MNPs in PBS buffer solution were exposed to alternating magnetic fields (AMFs) of 93.75 kHz or 104.5 kHz and B = 45 mT amplitude using a custom-made hyperthermia setup. Due to extensive cooling and mitigation of inductive losses in the electromagnet, this setup allows for accurate measurements of the MNPs' dissipated power. The total particle concentration in the sample was 35 µM, corresponding to 55 mg/mL and 16 % (w/w) of total metal ions. Figure 6 and Figure S4 show the average heating curves of three repeats for pure, Co7, or Zn7 MFts. From each measurement, the temperature kinetics of buffer measured under identical conditions was subtracted, yielding ΔT. Care was taken to measure each sample up to the steady-state condition during heating and cooling stages (10-15 min after switching the AMF on or off). At 93.75 kHz, the pure MFt sample exhibits a temperature increase above the buffer reference up to ΔT = 3.6 K during exposure to the AMF. The Zn7 sample exhibits a lower temperature increase of ΔT = 2.5 K during inductive heating. This lower response, however, is not significantly different in comparison to the pure MFt sample given the $\pm$2 K absolute temperature accuracy of the IR-camera. Single heating curves were highly robust, since repetitions were near identical and hence did not contribute to the uncertainty (see Figure 6A, where the coloured envelope indicates the error arising from repeat measurements). Intriguingly, Co7 samples led to an inductive heating of ΔT = 8 K after 300 s in AMF. Such significant temperature increase provides evidence, that doped MFts can act as heat mediators. At 104.5 kHz AMF frequency, all three MFt samples exhibited slightly lower heating rates compared to the measurement at 93.75 kHz (see Figure S4). While the pure MFt sample again heated up to ΔT_{max} = 3 K, the Zn7 sample

showed ΔT_{max} = 1.2 K and the Co7 sample ΔT_{max} = 6.1 K. Previous tests using horse spleen ferritin as a reference, led to no measurable heating,[28] corroborating our finding, that the synthesis of a particular magnetic core is critical to maximise the heating response.

The trend observed in the calorimetric experiments can be explained with their magnetic properties. In the linear response regime, the power losses are described by the specific absorption rate (SAR). It is proportional to the frequency, f, to the square of the external magnetic field amplitude, H_0, and to the out-of-phase component of the magnetic susceptibility, $\chi''(f)$:[81]

$$SAR \propto f\mu_0 H_0^2 \chi''(f).$$

χ'' depends non-linearly on f, increases with the MFt's magnetic moment, and reaches a maximum when the Néel relaxation time τ_N (*i.e.,* the magnetic moment reversal time above the energy barrier), matches the period of the alternating magnetic field. This latter condition is, in our experiments, best satisfied for the Co7 sample, with increased magnetic anisotropy as compared to pure and Zn7 samples.

Since all measurements were performed using identical settings, the slightly lower inductive heating in case of Co7 and Zn7 at 104.5 kHz could arise from a lower AC susceptibility, χ'', which is directly proportional to the dissipated power.

Our data reveals an overall low inductive heating of the MFts, which manifests itself in the SAR values per mass of total metal ions (see Figure 6B). The SAR was evaluated from the initial slope of the fit to the heating curves amounting to 6.7 ± 0.1 W·g^{-1} for pure MFt, 4.8 ± 0.2 W·g^{-1} for pure Zn7, and 25.7 ± 0.5 W·g^{-1} for Co7. The low inductive heating response and small SAR values are indeed expected for MNPs of this diameter[56,82]. SAR values are also low in comparison to data reported for larger MNPs in the literature[83–86] and our measurements using the same setup[65], typically amounting to ~100 W/g. However, the heat rate of the Co7 sample is the maximal value typically achieved for these types of magnetic cores measured under similar conditions[62] and is promising to promote or even initiate heat sensitive cellular processes in AMF. Moreover, the changes observed for different core doping and different frequency settings highlight, that the inductive heating response is dependent on the experimental design for which here optimised AMF excitation settings and core compositions are found. Co7 MFts could hence only act as mild heat mediators, when the nanoparticles are accumulated to high local concentrations (*e.g.,* 35 µM) resulting in the surrounding buffer solution to heat by 2-3 degrees per minute.

Finally, it should be noted, that all measurements were performed using external field parameters which fall below the physiological tolerance threshold.[87] Such settings are important, when biological measurements are envisaged, where physiologically serviceable power losses are required.

MFt Spatial Manipulation.

Since cell signalling processes were shown to rely on (i) the spatiotemporal regulation of molecular distribution[14,15] or (ii) on the application of mechanical forces,[16,18] we here provide examples, how synthesised MFts are useful in this biological context. In particular, we show how MFTs can be redistributed and accumulated in different intracellular compartments. On the one hand, this may be exploited for the (i) coupling of the MFts to signalling proteins and their active spatial redistribution to understand cell signalling processes. On the other hand, (ii) localised MFt accumulations may exert gentle forces to trigger mechanosensitive processes.

To explore the suitability of the MFts to respond to an applied magnetic field gradient, we first redistributed the MFts under idealised conditions, *i.e.,* using droplets of MFts in a glycerol/water (25:75 V/V) mixture on PDMS-coated glass coverslips. A home-made magnetic tip consisting of spring steel wire connected to Neodymium magnets was approached to the droplet (see Figure 7 and SI Video 1). The magnetic tip generated magnetic gradients on the order of $10^3 - 10^4$ T/m, as previously described. [17,32]

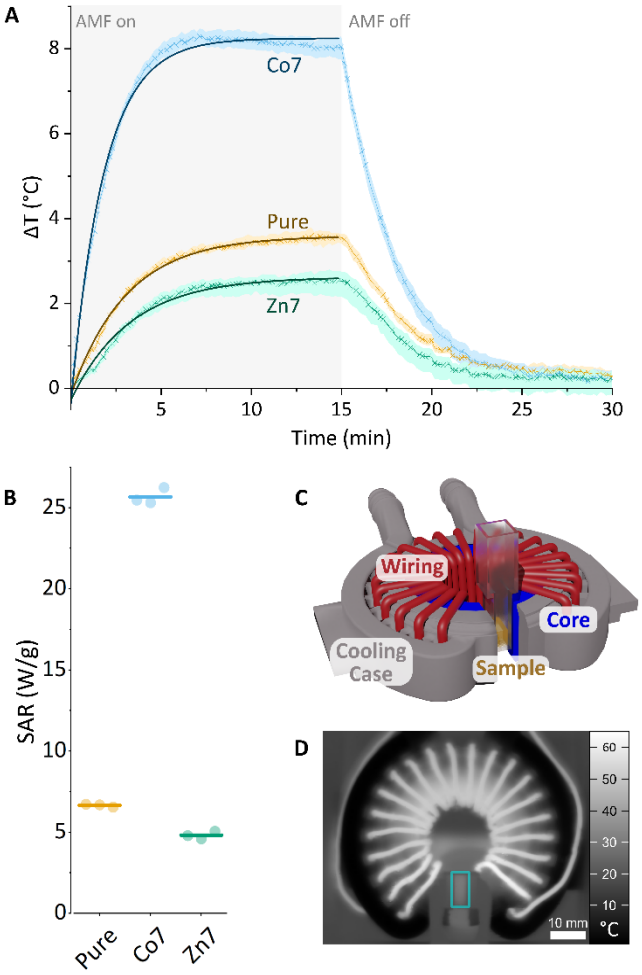

Figure 6 – (A) Hyperthermia measurement. Temperature kinetics of pure, Co7, and Zn7 MFt sample (each 35 µM) during exposure to the alternating magnetic field (45 mT, 93.75 kHz). Each curve is an average of three runs. The absolute temperature change ΔT refers to the temperature increase above the temperature of pure buffer solution. All MFt and buffer solution samples measured in an identical manner. (B) Specific Absorption Rate (W/g) of each run (coloured dot) and average value (coloured line). (C) Custom-made hyperthermia setup. (D) Selected thermal image of that was taken during hyperthermia measurement, with the sample (blue box) in the centre of the magnet gap.

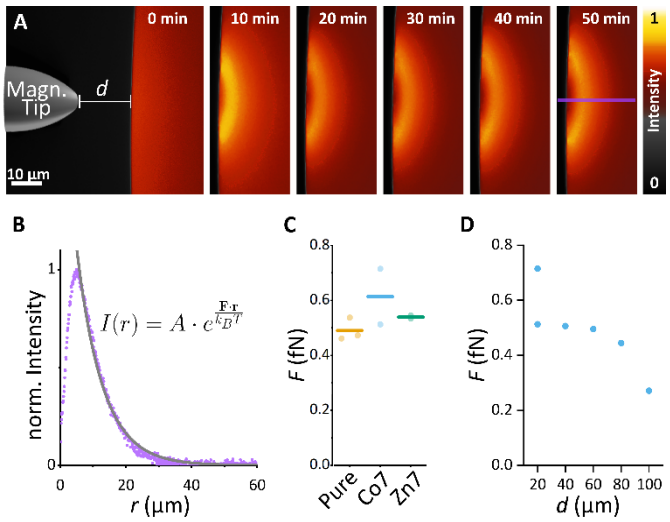

Figure 7 – Droplet assay with differently doped Magnetoferritin. (A) Exemplary assay with pure MFt. Magnetic tip was introduced at 0 min at a distance of 20 µm and left at the designated position for 50 min. (B) In the steady state, a line scan over 1 µm (purple line in A) was used to determine the force *F* affecting MFt using the displayed fit function. (C) Forces determined via droplet assay for all doping conditions. (D) Force – distance dependence for different distances *d* between droplet and magnetic tip using the Co7 MFt sample.

Together with the magnetic moment reported in the previous section, MFts should hence encounter forces in the femto-Newton regime. This is too weak to produce clear ballistic MNP trajectories toward the magnetic tip, instead the MNPs show a biased diffusion resulting from the superposition of a Brownian motion with a magnetic drift. When the magnetic tip was positioned at a particular distance d from the surface of the droplet, MFts were attracted towards the tip and formed a sharp gradient from the edge towards the centre of the droplet up to the distance, where the attractive magnetic potential was exceeded by the thermal Brownian motion (see Figure 7B). At steady state, the MNP distribution followed a Boltzmann distribution and was fitted with an approximate relation to determine the applied force $\boldsymbol{F}$:

$$I(\boldsymbol{r}) = A \cdot \exp\left(\frac{\boldsymbol{F}\cdot\boldsymbol{r}}{k_\mathrm{B}T}\right).$$

I is the intensity distribution along the purple line in Figure 7A, A is the amplitude, k_B the Boltzmann constant, T the temperature, and $\boldsymbol{r}$ the radial distance from the tip. Here, it was assumed that the droplet size is sufficiently small to have a constant magnetic force $\boldsymbol{F}$ across the droplet diameter, albeit the magnetic force $\boldsymbol{F}$ decreases as $1/r^2$ for a parabolic tip.[88,89] Figure 7B shows the steady state MNP distributions of the pure sample along with the intensity profile fit as an example. Similar distributions were obtained for the MFt with dopant and were fitted accordingly. The forces are $F_\mathrm{pure} = 0.49$ fN, $F_\mathrm{Co7} = 0.61$ fN, and $F_\mathrm{Zn7} = 0.54$ fN. This data confirms the mentioned theoretical estimate of fN forces generated by the current setup. In contrast to the hyperthermia results, no significant difference in the magnetic response between the different MFts was observed. This is reasonable, given the magnetic moments derived from the Langevin fit to the magnetisation curves vary only by 5 % for MFt and Co7. In addition, differences in the magnetic field gradient sensitively depend on the lateral MFt – tip distance, which may vary by a few 100 nm between the samples. In order to probe the force variation with the droplet-tip distance, the steady-state MFt distribution was further analysed, placing the magnetic tip 20 to 100 µm away from the tip. Interestingly, MFt attraction was visible over the whole range up to the 100 µm droplet-tip distance. This is an important prerequisite when magnetic manipulation approaches at a distance, *e.g.,* through a glass cover slip, are envisaged. At 100 µm distances, a magnetic force of $F_\mathrm{Co7} = 0.27$ fN was derived. In summary, the MFt droplet assay confirmed the ability to generate tuneable and reversible MFt profiles. To further demonstrate the suitability of the MFts to be spatially redistributed within a subcellular compartment, we microinjected Co7 MFts into the cell cytoplasm or in the cell nucleus (see Figure 8 and SI Videos 2 and 3). The same type of magnetic tip as used for the droplet assay, was approached to the cell from different sites. MFts were quickly attracted in the direction of the magnetic tip and formed µm size areas of strong MFt accumulation. A steady state distribution was typically reached after 5 min and the magnetic tip was removed to show the reversible MFt diffusion. When MFts were manipulated in the cell cytoplasm (see Figure 8A-C), particles were already attracted when the tip was placed about 70 µm away from the cell edge. At short distances from the cell edge (~10 µm), strong MFt accumulations developed. When the magnetic tip was moved to different sites of the cell, the MFts were immediately redistributed. MFts remained mobile and did not form any agglomerations during field-assisted manipulation. They fully dispersed in the cell cytoplasm after removal of the magnetic tip. MFt manipulation in general did not lead to any microscopic deformations of the cell shape. Yet, in case of strong MFt accumulation and attraction over several minutes, after tip removal and MFt dispersion, a slight increase in the projected fluorescence intensity at the manipulation site compared to the initial state was observed. This suggested that an increase in the cytoplasmic volume can occur along with a displacement of intracellular structures, when high local MFt concentrations are present. When MFts were manipulated in the cell nucleus (see Figure 8D-F), particles were reversibly attracted inside the nucleus, without observing any intensity change after the manipulation. Interestingly, the attraction was fully reversible and MFts remained inside the nucleus, without any detectable escape to the cell cytoplasm. The spatial manipulation of MFts can hence serve as a tool to actively redistribute MFt coupled molecules for cell signalling studies. It may also be used to apply gentle mechanical stimuli to intracellular structures depending on the magnetic field gradient and the magnetic flux density applied.

Conclusion & Outlook

We have demonstrated that ferritin-based magnetic nanoparticles (MFts) offer a versatile platform for spatial magnetic manipulation approaches, whereas an inductive heating of the nanoparticles is possible only for optimal alternating magnetic field settings and mineralised cores of high

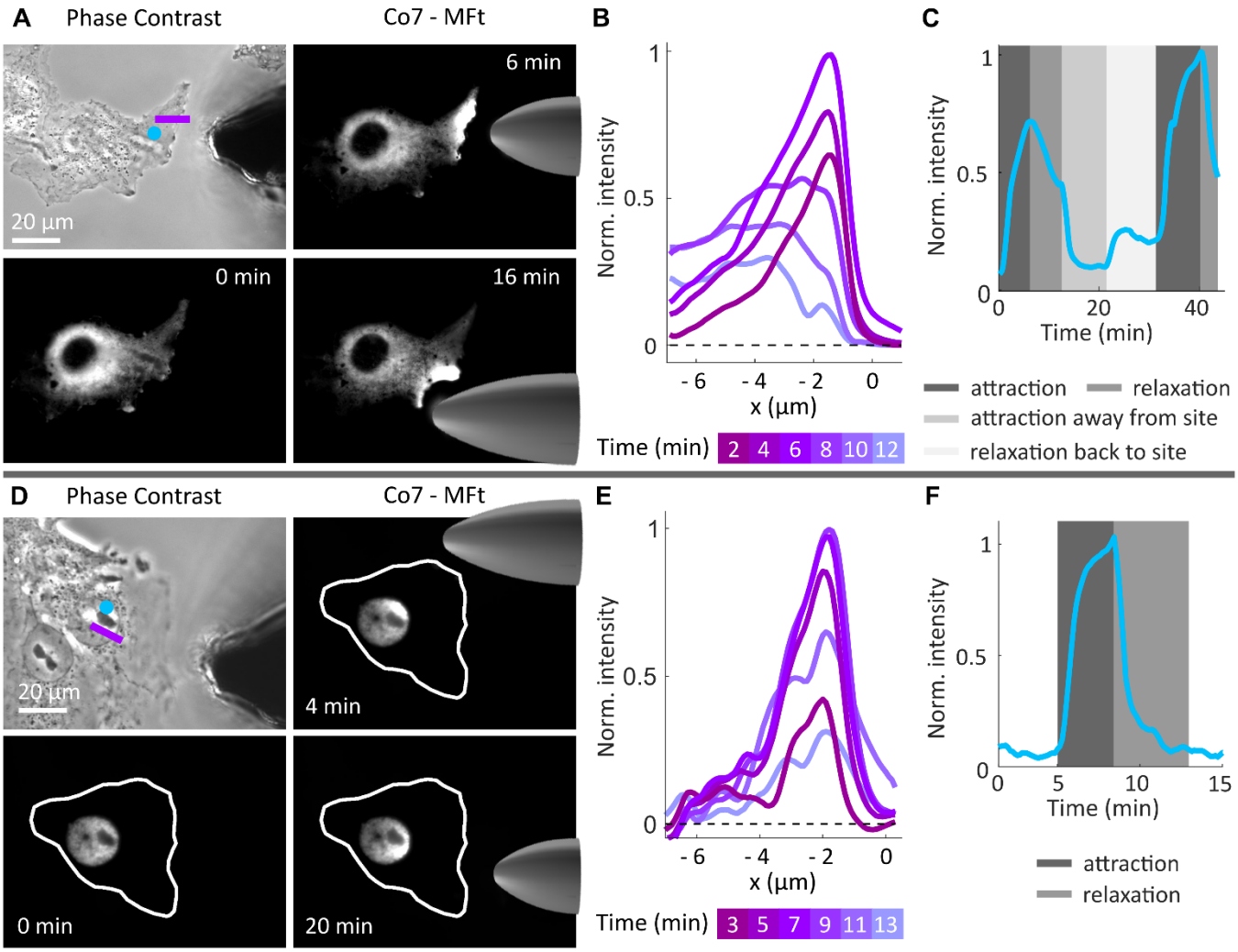

Figure 8 – Spatial Manipulation of Magnetoferritin in Cells. (A) Phase Contrast Image of Cos7 cell and micromagnetic tip. Fluorescence image of Co7-MFt spatial redistribution in the cell cytoplasm placing the magnetic tip at different positions. (B) Fluorescence intensity profile along the pink line in (A) during attraction (2-6 min) and relaxation (8-12 min). (C) Average fluorescence intensity within the blue spot in (A) over time. The intensity increases and decreases according to the spatial manipulation mode. (D) Phase Contrast Image of Cos7 cell and micromagnetic tip. Fluorescence image of Co7-MFt spatial redistribution in the cell nucleus placing the magnetic tip at different positions. (E) Fluorescence intensity profile along the pink line in (D) during attraction (3-10 min) and relaxation (11-13 min). (F) Average fluorescence intensity within the blue spot in (D) over time. The intensity profile exhibits the characteristic exponential increase and decrease during attraction and relaxation, respectively. In (B) and (E) the background intensity profile was subtracted from the data and spatial averaging performed over a line with a width of 5 pixel.

magnetic anisotropy (*e.g.,* Co doped cores). In particular, we synthesised a bioengineered ferritin based magnetic nanoparticle (MNP) exhibiting mEGFP and PEG coupled to its surface. This enabled to track the particle as well as to prevent any unspecific interaction of the particle within a synthetic or cellular environment. Three types of MFts were synthesised with an undoped, 7 % Zn- or 7 % Co doped superparamagnetic core with high size homogeneity of the shell and core. Thus, MFts are addressable one particle at a time and allow to transmit the same magnetic stimulus, an important prerequisite for many bio- and nanotechnological applications.

7 % Cobalt doping yielded the highest effective magnetic anisotropy and significantly improved the hyperthermic heat performance. Here, inductive heating experiments at 93.75 kHz resulted in temperatures of 8 K above a buffer reference within a few minutes. This provided evidence that Co doped MFts can act as a mild heat mediator when optimised magnetic field settings and nanoparticle core properties are used. 7 % Zinc doping and the pure mineral core resulted in superparamagnetism down to $\leq$ 60 K, and measurements at different frequencies only brought about a little heating effect. Our rigorous measurements provide new insights to the recent discussion, whether (or under which conditions) MFts can act as heat mediators.

Next to probing the MFt applicability for magnetic hyperthermia, their suitability for spatial manipulation approaches in a biological context was tested. Here, all MFts performed very well and comparable in terms of their spatial redistribution potential. The MFts were reversibly attracted in droplets or inside cells approaching a magnetic tip (*i.e.,* a magnetic field gradient) and attraction forces were easily modulated by changing the MFt – magnetic tip distance. In

agreement with theoretical calculations, the analysis of experimentally obtained MNP distributions revealed, that nanoparticles exert mild forces in the fN regime. The MFts could hence be used to couple molecules to the MFt surface, to (i) spatially redistribute the molecules to create local signalling hubs, (ii) to switch their (conformational) activity state, or (iii) to exploit the biological mechano-sensitivity in a mild force transduction approach without compromising the biological environment. In conclusion, the Co doped MFt is an extremely versatile and small functionalised targeting nanosystem, which offers the best magnetic properties for a spatial or force mediated manipulation of individual molecules along with some potential for nanotechnological hyperthermia applications.

Author Contributions

Conceptualisation: AN, CM, UW
Methodology: AN, CM, DAK, IPN, NT, SS, PH, UW
Investigation: AN, CM, DAK, UW
Visualisation: AN, CM, DAK, UW
Supervision: CM, UW, MF
Writing-original draft: AN, CM, DAK, UW

Conflicts of interest

There are no conflicts of interest to declare.

Acknowledgements

C M acknowledges financial support of the Deutsche Forschungsgemeinschaft (DFG, German Research Foundation) through CRC1208 'Identity and Dynamics of Membrane Systems' (A12, Project ID 267205415) and CRC1535 'Microbial Networks' (A09, Project ID 458090666). C M and A N acknowledge financial support via the 'Freigeist fellowship' of VolkswagenFoundation. The authors acknowledge the DFG and the State of North Rhine–Westphalia for funding the cryo-TEM (INST 208/749-1 FUGG) hosted by the Centre of Advanced Imaging (CAi, Heinrich-Heine University). We thank the group of Prof. Claus Seidel (Physical Chemistry, Heinrich-Heine University) for providing lab space and laboratory equipment, the group of Prof. Lutz Schmitt (Biochemistry, Heinrich-Heine University) for providing the cell disruptor, and the group of Prof. Laura Hartmann (Macromolecular Chemistry, Heinrich-Heine University) for providing the Zetasizer.

Notes and references

1 Z. Yuan, B. Wang, Y. Teng, W. Ho, B. Hu, K. O. Boakye-Yiadom, X. Xu and X.-Q. Zhang, *Nanoscale*, 2022, **14**, 6449–6464.

2 I. Inoue, M. Chiba, K. Ito, Y. Okamatsu, Y. Suga, Y. Kitahara, Y. Nakahara, Y. Endo, K. Takahashi, U. Tagami and N. Okamoto, *Nanoscale*, 2021, **13**, 1875–1883.

3 X. Lin, J. Xie, G. Niu, F. Zhang, H. Gao, M. Yang, Q. Quan, M. A. Aronova, G. Zhang, S. Lee, R. Leapman and X. Chen, *Nano Lett.*, 2011, **11**, 814–819.

4 K. Fan, C. Cao, Y. Pan, D. Lu, D. Yang, J. Feng, L. Song, M. Liang and X. Yan, *Nat. Nanotechnol.*, 2012, **7**, 459–464.

5 K. Li, Z. P. Zhang, M. Luo, X. Yu, Y. Han, H. P. Wei, Z. Q. Cui and X. E. Zhang, *Nanoscale*, 2012, **4**, 188–193.

6 C. Massner, F. Sigmund, S. Pettinger, M. Seeger, C. Hartmann, N. P. Ivleva, R. Niessner, H. Fuchs, M. H. de Angelis, A. Stelzl, N. L. Koonakampully, H. Rolbieski, U. Wiedwald, M. Spasova, W. Wurst, V. Ntziachristos, M. Winklhofer and G. G. Westmeyer, *Adv. Funct. Mater.*, 2018, **28**, 1706793.

7 H. J. Kang, Y. J. Kang, Y. M. Lee, H. H. Shin, S. J. Chung and S. Kang, *Biomaterials*, 2012, **33**, 5423–5430.

8 Z. Wang, Y. Dai, Z. Wang, O. Jacobson, F. Zhang, B. C. Yung, P. Zhang, H. Gao, G. Niu, G. Liu and X. Chen, *Nanoscale*, 2018, **10**, 1135–1144.

9 E. Fantechi, C. Innocenti, M. Zanardelli, M. Fittipaldi, E. Falvo, M. Carbo, V. Shullani, L. Di Cesare Mannelli, C. Ghelardini, A. M. Ferretti, A. Ponti, C. Sangregorio and P. Ceci, *ACS Nano*, 2014, **8**, 4705–4719.

10 R. Chen, G. Romero, M. G. Christiansen, A. Mohr and P. Anikeeva, *Science*, 2015, **347**, 1477–1480.

11 K. Ohara, T. Moriwaki, K. Nakazawa, T. Sakamoto, K. Nii, M. Abe and Y. Ichiyanagi, *AIP Adv.*, 2023, **13**, 025238.

12 F. Etoc, D. Lisse, Y. Bellaiche, J. Piehler, M. Coppey and M. Dahan, *Nat. Nanotechnol.*, 2013, **8**, 193–198.

13 F. Etoc, C. Vicario, D. Lisse, J. M. Siaugue, J. Piehler, M. Coppey and M. Dahan, *Nano Lett.*, 2015, **15**, 3487–3494.

14 M. Aubry, W. A. Wang, Y. Guyodo, E. Delacou, J. M. Guigner, O. Espeli, A. Lebreton, F. Guyot and Z. Gueroui, *ACS Synth. Biol.*, 2020, **9**, 3030–3041.

15 Y. Shi, L. Huang, H. Dong, M. Yang, W. Ding, X. Zhou, T. Lu, Z. Liu, X. Zhou, M. Wang, B. Zeng, Y. Sun, S. Zhong, B. Wang, W. Wang, C. Yin, X. Wang and Q. Wu, *Cell Res.*, 2024, **34**, 193–213.

16 D. Seo, K. M. Southard, J. W. Kim, H. J. Lee, J. Farlow, J. U. Lee, D. B. Litt, T. Haas, A. P. Alivisatos, J. Cheon, Z. J. Gartner and Y. W. Jun, *Cell*, 2016, **165**, 1507–1518.

17 D. Lißе, C. Monzel, C. Vicario, J. Manzi, I. Maurin, M. Coppey, J. Piehler and M. Dahan, *Adv. Mater.*, 2017, **29**, 1–7.

18 C. Monzel, C. Vicario, J. Piehler, M. Coppey and M. Dahan, *Chem. Sci.*, 2017, **8**, 7330–7338.

19 A. S. Garanina, M. V. Efremova, A. E. Machulkin, E. V. Lyubin, N. S. Vorobyeva, O. A. Zhironkina, O. S. Strelkova, I. I. Kireev, I. B. Alieva, R. E. Uzbekov, V. N. Agafonov, I. V. Shchetinin, A. A. Fedyanin, A. S. Erofeev, P. V. Gorelkin, Y. E. Korchev, A. G. Savchenko and M. A. Abakumov, *Magnetochemistry*, 2022, **8**, 185.

20 A. K. Gupta and M. Gupta, *Biomaterials*, 2005, **26**, 3995–4021.

21 Y. Zhu, Y. Zhu, T. Cao, X. Liu, X. Liu, Y. Yan, Y. Shi and J. C. Wang, *Med. Rev.*, 2023, **3**, 49–74.

22 D. He and J. Marles-Wright, *N. Biotechnol.*, 2015, **32**, 651–657.

23 M. Kumar, J. Markiewicz-Mizera, J. D. Janna Olmos, P. Wilk, P. Grudnik, A. P. Biela, M. Jemioła-Rzemińska, A. Górecki, S.

Chakraborti and J. G. Heddle, *Nanoscale*, 2021, **13**, 11932–11942.
24 Y. Jin, J. He, K. Fan and X. Yan, *Nanoscale*, 2019, **11**, 12449–12459.
25 A. Mohanty, A. Parida, R. K. Raut and R. K. Behera, *ACS Bio Med Chem Au*, 2022, **2**, 258–281.
26 A. N. Gabashvili, S. S. Vodopyanov, N. S. Chmelyuk, V. A. Sarkisova, K. A. Fedotov, M. V. Efremova and M. A. Abakumov, *Int. J. Mol. Sci.*, 2021, **22**, 12275.
27 M. Meister, *eLife*, 2016, **5**, 1–14.
28 H. C. Davis, S. Kang, J. H. Lee, T. H. Shin, H. Putterman, J. Cheon and M. G. Shapiro, *Biophys. J.*, 2020, **118**, 1502–1510.
29 Y. Zhang and B. P. Orner, *Int. J. Mol. Sci.*, 2011, **12**, 5406–5421.
30 P. M. Harrison and P. Arosio, *Biochim. Biophys. Acta - Bioenerg.*, 1996, **1275**, 161–203.
31 E. Fantechi, C. Innocenti, M. Zanardelli, M. Fittipaldi, E. Falvo, M. Carbo, V. Shullani, L. Di Cesare Mannelli, C. Ghelardini, A. M. Ferretti, A. Ponti, C. Sangregorio and P. Ceci, *ACS Nano*, 2014, **8**, 4705–4719.
32 I. P. Novoselova, A. Neusch, J. S. Brand, M. Otten, M. R. Safari, N. Bartels, M. Karg, M. Farle, U. Wiedwald and C. Monzel, *Nanomaterials*, 2021, **11**, 1–20.
33 E. Falvo, E. Tremante, R. Fraioli, C. Leonetti, C. Zamparelli, A. Boffi, V. Morea, P. Ceci and P. Giacomini, *Nanoscale*, 2013, **5**, 12278–12285.
34 D. Liße, C. P. Richter, C. Drees, O. Birkholz, C. You, E. Rampazzo and J. Piehler, *Nano Lett.*, 2014, **14**, 2189–2195.
35 X. Li, L. Qiu, P. Zhu, X. Tao, T. Imanaka, J. Zhao, Y. Huang, Y. Tu and X. Cao, *Small*, 2012, **8**, 2505–2514.
36 F. Etoc, D. Lisse, Y. Bellaiche, J. Piehler, M. Coppey and M. Dahan, *Nat. Nanotechnol.*, 2013, **8**, 193–198.
37 F. Raudzus, H. Schöneborn, S. Neumann, E. Secret, A. Michel, J. Fresnais, O. Brylski, C. Ménager, J. M. Siaugue and R. Heumann, *Sci. Rep.*, 2020, **10**, 22452.
38 M. Le Jeune, E. Secret, M. Trichet, A. Michel, D. Ravault, F. Illien, J.-M. Siaugue, S. Sagan, F. Burlina and C. Ménager, *ACS Appl. Mater. Interfaces*, 2022, **14**, 15021–15034.
39 N. K. Lee, S. Cho and I. S. Kim, *Exp. Mol. Med.*, 2022, **54**, 1652–1657.
40 N. Aronovitz, M. Neeman and R. Zarivach, in *Iron Oxides*, ed. D. Faivre, John Wiley & Sons, Ltd, Hoboken, 2016, pp. 117–142.
41 E. C. Theil, *Adv. Enzymol. Relat. Areas Mol. Biol.*, 1990, **63**, 421–449.
42 A. García-Prieto, J. Alonso, D. Muñoz, L. Marcano, A. Abad Díaz de Cerio, R. Fernández de Luis, I. Orue, O. Mathon, A. Muela and M. L. Fdez-Gubieda, *Nanoscale*, 2016, **8**, 1088–1099.
43 M. A. Kostiainen, P. Ceci, M. Fornara, P. Hiekkataipale, O. Kasyutich, R. J. M. Nolte, J. J. L. M. Cornelissen, R. D. Desautels and J. Van Lierop, *ACS Nano*, 2011, **5**, 6394–6402.
44 M. A. Kostiainen, P. Hiekkataipale, A. Laiho, V. Lemieux, J. Seitsonen, J. Ruokolainen and P. Ceci, *Nat. Nanotechnol.*, 2013, **8**, 52–56.
45 S. Gider, D. D. Awschalom, T. Douglas, S. Mann and M. Chaparala, *Science*, 1995, **268**, 77–80.
46 Q. A. Pankhurst, S. Betteridge, D. P. E. Dickson, T. Douglas, S. Mann and R. B. Frankel, *Hyperfine Interact.*, 1994, **91**, 847–851.
47 M. Allen, D. Willits, M. Young and T. Douglas, *Inorg. Chem.*, 2003, **42**, 6300–6305.
48 D. A. Resnick, K. Gilmore, Y. U. Idzerda, M. T. Klem, M. Allen, T. Douglas, E. Arenholz and M. Young, *J. Appl. Phys.*, 2006, **99**, 2006–2008.
49 P. Mackle, J. M. Charnock, C. D. Garner, F. C. Meldrum and S. Mann, *J. Am. Chem. Soc.*, 1993, **115**, 8471–8472.
50 B. Warne, O. I. Kasyutich, E. L. Mayes, J. A. L. Wiggins and K. K. W. Wong, *IEEE Trans. Magn.*, 2000, **36**, 3009–3011.
51 T. Ueno, M. Suzuki, T. Goto, T. Matsumoto, K. Nagayama and Y. Watanabe, *Angew. Chemie Int. Ed.*, 2004, **43**, 2527–2530.
52 R. M. Kramer, C. Li, D. C. Carter, M. O. Stone and R. R. Naik, *J. Am. Chem. Soc.*, 2004, **126**, 13282–13286.
53 K. K. W. Wong and S. Mann, *Adv. Mater.*, 1996, **8**, 928–932.
54 I. Yamashita, J. Hayashi and M. Hara, *Chem. Lett.*, 2004, **33**, 1158–1159.
55 K. Iwahori, K. Yoshizawa, M. Muraoka and I. Yamashita, *Inorg. Chem.*, 2005, **44**, 6393–6400.
56 J. P. Fortin, C. Wilhelm, J. Servais, C. Ménager, J. C. Bacri and F. Gazeau, *J. Am. Chem. Soc.*, 2007, **129**, 2628–2635.
57 M. Gonzales-Weimuller, M. Zeisberger and K. M. Krishnan, *J. Magn. Magn. Mater.*, 2009, **321**, 1947–1950.
58 L. Lartigue, C. Innocenti, T. Kalaivani, A. Awwad, M. D. M. Sanchez Duque, Y. Guari, J. Larionova, C. Gueírin, J. L. G. Montero, V. Barragan-Montero, P. Arosio, A. Lascialfari, D. Gatteschi and C. Sangregorio, *J. Am. Chem. Soc.*, 2011, **133**, 10459–10472.
59 M. V. Efremova, Y. A. Nalench, E. Myrovali, A. S. Garanina, I. S. Grebennikov, P. K. Gifer, M. A. Abakumov, M. Spasova, M. Angelakeris, A. G. Savchenko, M. Farle, N. L. Klyachko, A. G. Majouga and U. Wiedwald, *Beilstein J. Nanotechnol.*, 2018, **9**, 2684–2699.
60 M. Comes Franchini, G. Baldi, D. Bonacchi, D. Gentili, G. Giudetti, A. Lascialfari, M. Corti, P. Marmorato, J. Ponti, E. Micotti, U. Guerrini, L. Sironi, P. Gelosa, C. Ravagli and A. Ricci, *Small*, 2010, **6**, 366–370.
61 E. Skoropata, R. D. Desautels, E. Falvo, P. Ceci, O. Kasyutich, J. W. Freeland and J. Van Lierop, *Phys. Rev. B*, 2014, **90**, 174424.
62 R. Das, N. P. Kim, S. B. Attanayake, M.-H. Phan and H. Srikanth, *Appl. Sci.*, 2021, **11**, 930.
63 S. Singhal, T. Namgyal, S. Bansal and K. Chandra, *J. Electromagn. Anal. Appl.*, 2010, **2**, 376–381.
64 D. S. Mathew and R. S. Juang, *Chem. Eng. J.*, 2007, **129**, 51–65.
65 D. A. Kuckla, J.-S. Brand, B. Czech, A. Asharion, J. V. Jüttner, I. P. Novoselova, A. Neusch, P. Hagemann, M. Getzlaff and C. Monzel, *J. Phys. D. Appl. Phys.*, 2023, **56**, 505002.
66 A. L. Thangawng, R. S. Ruoff, M. A. Swartz and M. R. Glucksberg, *Biomed. Microdevices*, 2007, **9**, 587–595.
67 J. Schindelin, I. Arganda-Carreras, E. Frise, V. Kaynig, M.

Longair, T. Pietzsch, S. Preibisch, C. Rueden, S. Saalfeld, B. Schmid, J. Y. Tinevez, D. J. White, V. Hartenstein, K. Eliceiri, P. Tomancak and A. Cardona, *Nat. Methods*, 2012, **9**, 676–682.

68 M. G. Christiansen, N. Mirkhani, W. Hornslien and S. Schuerle, *J. Appl. Phys.*, 2022, **132**, 174304.

69 M. A. Hink, R. A. Griep, J. W. Borst, A. Van Hoek, M. H. M. Eppink, A. Schots and A. J. W. G. Visser, *J. Biol. Chem.*, 2000, **275**, 17556–17560.

70 F. Etoc, E. Balloul, C. Vicario, D. Normanno, D. Liße, A. Sittner, J. Piehler, M. Dahan and M. Coppey, *Nat. Mater.*, 2018, **17**, 740–746.

71 J. I. Langford and A. J. C. Wilson, *J. Appl. Crystallogr.*, 1978, **11**, 102–113.

72 K. Zeth, E. Hoiczyk and M. Okuda, *Trends Biochem. Sci.*, 2016, **41**, 190–203.

73 V. A. Drits, B. A. Sakharov, A. L. Salyn and A. Manceau, *Clay Miner.*, 1993, **28**, 185–207.

74 E. Jansen, A. Kyek, W. Schäfer and U. Schwertmann, *Appl. Phys. A Mater. Sci. Process.*, 2002, **74**, 1004–1006.

75 W. Kim, C. Y. Suh, S. W. Cho, K. M. Roh, H. Kwon, K. Song and I. J. Shon, *Talanta*, 2012, **94**, 348–352.

76 Y. A. Nalench, I. V. Shchetinin, A. S. Skorikov, P. S. Mogilnikov, M. Farle, A. G. Savchenko, A. G. Majouga, M. A. Abakumov and U. Wiedwald, *J. Mater. Chem. B*, 2020, **8**, 3886–3895.

77 P. Saha, R. Rakshit, M. Alam and K. Mandal, *Phys. Rev. Appl.*, 2019, **11**, 024059.

78 S. Liébana-Viñas, K. Simeonidis, U. Wiedwald, Z.-A. Li, Z. Ma, E. Myrovali, A. Makridis, D. Sakellari, G. Vourlias, M. Spasova, M. Farle and M. Angelakeris, *RSC Adv.*, 2016, **6**, 72918–72925.

79 L. Néel, *Ann. géophysique*, 1949, **5**, 99–136.

80 M. T. Klem, D. A. Resnick, K. Gilmore, M. Young, Y. U. Idzerda and T. Douglas, *J. Am. Chem. Soc.*, 2007, **129**, 197–201.

81 Q. A. Pankhurst, J. Connolly, S. K. Jones and J. Dobson, *J. Phys. D. Appl. Phys.*, 2003, **36**, R167–R181.

82 S. Purushotham and R. V. Ramanujan, *J. Appl. Phys.*, 2010, **107**, 114701.

83 A. Lascialfari, M. Filibian, C. Sangregorio and P. Carretta, *La Riv. del Nuovo Cim.*, 2013, **36**, 211–271.

84 P. Guardia, R. Di Corato, L. Lartigue, C. Wilhelm, A. Espinosa, M. Garcia-Hernandez, F. Gazeau, L. Manna and T. Pellegrino, *ACS Nano*, 2012, **6**, 3080–3091.

85 J.-H. Lee, J. Jang, J. Choi, S. H. Moon, S. Noh, J. Kim, J.-G. Kim, I.-S. Kim, K. I. Park and J. Cheon, *Nat. Nanotechnol.*, 2011, **6**, 418–422.

86 H. Gavilán, K. Simeonidis, E. Myrovali, E. Mazarío, O. Chubykalo-Fesenko, R. Chantrell, L. Balcells, M. Angelakeris, M. P. Morales and D. Serantes, *Nanoscale*, 2021, **13**, 15631–15646.

87 R. Hergt and S. Dutz, *J. Magn. Magn. Mater.*, 2007, **311**, 187–192.

88 T. Häberle, F. Haering, H. Pfeifer, L. Han, B. Achinuq, U. Wiedwald, U. Herr and B. Koslowski, *New J. Phys.*, 2012, **14**, 043044.

89 A. H. B. De Vries, B. E. Krenn, R. Van Driel and J. S. Kanger, *Biophys. J.*, 2005, **88**, 2137–2144.